GDCh

**Research Articles**

*Angewandte*
Chemie
International Edition
www.angewandte.org

*Layered Double Hydroxides*

# Revealing the Formation Mechanism and Optimizing the Synthesis Conditions of Layered Double Hydroxides for the Oxygen Evolution Reaction

*Zongkun Chen[+],\* Xingkun Wang[+], Zhongkang Han[+], Siyuan Zhang, Simone Pollastri, Qiqi Fan, Zhengyao Qu, Debalaya Sarker, Christina Scheu, Minghua Huang,\* and Helmut Cölfen\**

**Abstract:** Layered double hydroxides (LDHs), whose formation is strongly related to $OH^-$ concentration, have attracted significant interest in various fields. However, the effect of the real-time change of $OH^-$ concentration on LDHs' formation has not been fully explored due to the unsuitability of the existing synthesis methods for in situ characterization. Here, the deliberately designed combination of $NH_3$ gas diffusion and in situ pH measurement provides a solution to the above problem. The obtained results revealed the formation mechanism and also guided us to synthesize a library of LDHs with the desired attributes in water at room temperature without using any additives. After evaluating their oxygen evolution reaction performance, we found that FeNi-LDH with a Fe/Ni ratio of 25/75 exhibits one of the best performances so far reported.

## Introduction

Layered double hydroxides (LDHs) are a large family of two-dimensional materials with the general formula of $[M^{2+}_{1-x}M^{3+}_x(OH)_2]^{x+}[A^{n-}_{x/n}]^{x-}\cdot mH_2O$, where M and $A^{n-}$ are metal cations and the interlayered anions, respectively.[1] Due to their unique physicochemical properties,[1a–c] LDHs are considered as attractive materials for many applications.[1a,2] Accordingly, great efforts have been made to synthesize LDHs, which is mainly via various wet chemical strategies including hydrothermal/solvothermal method,[3] co-precipitation,[2b] electrodeposition,[2d,4] and microwave-assisted synthesis,[1a] etc. Wet chemical synthesis of LDHs is a precipitation process involving both, the reaction of M with $OH^-$ and the incorporation of doping M into the host lattice. Although it is well established that the nucleation and growth of the precipitate are strongly related to $OH^-$ concentration,[1a,5] progress is slow in understanding

the effect of the change of $OH^-$ concentration on the formation of LDHs, especially on the incorporation mechanism, because the existing synthesis methods are not ideal for realizing in situ monitoring of the change of $OH^-$ concentration.[5c] In fact, solving the above-mentioned problem is crucial not only to extend the understanding of the influence of $OH^-$ change on the morphology or crystallinity of LDHs and then design the synthesis scheme for the desired LDHs,[6] but also to optimize the synthesis conditions of LDHs via excluding undesired factors of the synthesis process.[1e,3,7]

Enlighted by the efficient crystallization control of the vapor diffusion method employed in our previous works,[8] we herein utilized a gas diffusion method, which involves the diffusion of $NH_3$ into an aqueous solution of $Ni^{2+}$ and $Fe^{2+/3+}$, to monitor the change of $OH^-$ via in situ pH measurement. Meanwhile, some reference experiments were also carried out using NaOH as the alkali source. We

[*] Dr. Z. Chen,[+] Q. Fan, Prof. H. Cölfen
University of Konstanz
78457 Konstanz (Germany)
E-mail: zongkun.chen@uni-konstanz.de
helmut.coelfen@uni-konstanz.de

X. Wang,[+] Prof. M. Huang
School of Materials Science and Engineering, Ocean University of China
266100 Qingdao (China)
E-mail: huangminghua@ouc.edu.cn

Dr. Z. Han,[+] D. Sarker
Fritz-Haber-Institut der Max-Planck-Gesellschaft
14195 Berlin (Germany)

Dr. S. Zhang, Prof. C. Scheu
Max-Planck-Institut für Eisenforschung GmbH
40237 Düsseldorf (Germany)

Dr. S. Pollastri
Elettra-Sincrotrone Trieste
Basovizza, Trieste (Italy)

Dr. Z. Qu
Agency for Science, Technology and Research
Singapore 138634 (Singapore)

[+] These authors contributed equally to this work.

selected FeNi-LDHs as a model material because: First, FeNi-LDHs and its derivative materials[9] are regarded as the most promising electrocatalysts for the oxygen evolution reaction (OER) in alkaline solutions.[2f, 7c, 10] Second, the Fe precursor ($Fe^{2+}$ or $Fe^{3+}$) is adjustable, which is beneficial for performing systematic research on the formation mechanism of LDHs. The disclosed results guided us to successfully synthesized various LDHs, namely FeNi-LDHs with different Fe/Ni ratios and other LDHs systems (FeY, CoNi, CoY, and CoNiY), in water under ambient conditions without using any additives, which is a significant improvement over previous methods. To verify optimizing the synthesis condition of LDHs without sacrificing their performance, all obtained LDHs were tested for OER in a 1.0 M KOH solution. In particular, FeNi-LDH with a Fe/Ni ratio of 25/75 exhibits excellent performance, which is reflected by ultralow overpotentials of 203 mV at 10 mA cm$^{-2}$, a Tafel slope of 24.9 mV dec$^{-1}$, and remaining nearly constant in the stability test. A combination of experimental characterization and density-functional theory (DFT) calculations reveals that the key to this remarkable electrocatalytic performance is the local electronic structure change of Ni sites caused by the incorporation of Fe species.

## Results and Discussion

Scheme 1 depicts the designed four reaction routes, in which $NH_3$ or NaOH was introduced into an aqueous solution of $Ni^{2+}$ and $Fe^{2+/3+}$ at ambient conditions without using any additives, and the obtained products were denoted as $NH_3$-$Fe^{2+}Ni^{2+}$, $NH_3$-$Fe^{3+}Ni^{2+}$, NaOH-$Fe^{2+}Ni^{2+}$, and NaOH-$Fe^{3+}Ni^{2+}$, respectively. As shown in the scanning electron microscopy (SEM) images (Figure S1A–D), $NH_3$-$Fe^{2+}Ni^{2+}$ and $NH_3$-$Fe^{3+}Ni^{2+}$ exhibit a hexagon nanosheet morphology with a diameter of around 200 nm, while aggregated small irregular nanosheets can be observed for NaOH-$Fe^{2+}Ni^{2+}$ and NaOH-$Fe^{3+}Ni^{2+}$. Furthermore, transmission electron microscopy (TEM) images (Figure 1A–D) confirm the
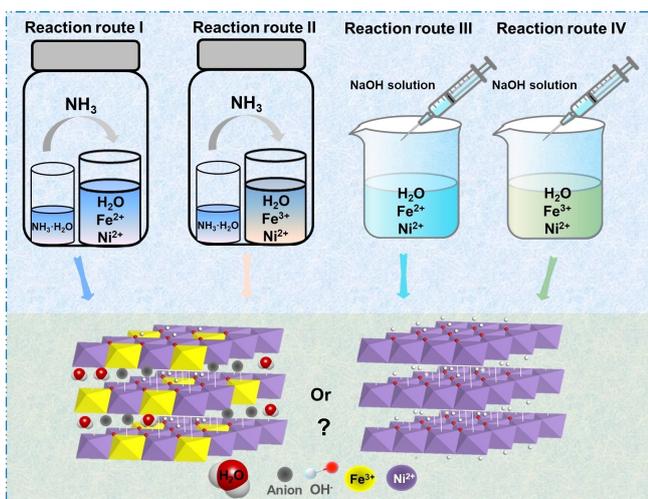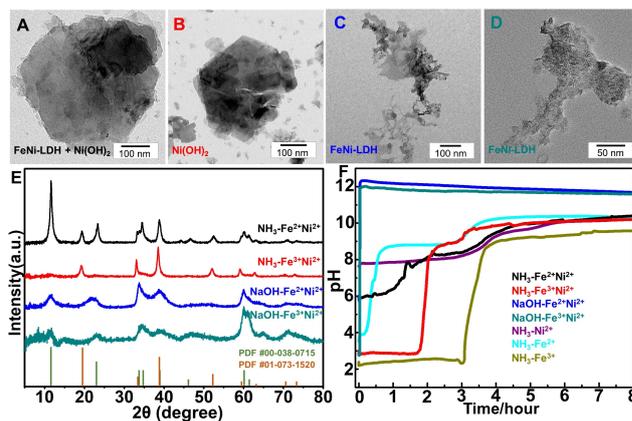


**Figure 1.** A)–D) TEM images and E) XRD patterns of $NH_3$-$Fe^{2+}Ni^{2+}$, $NH_3$-$Fe^{3+}Ni^{2+}$, NaOH-$Fe^{2+}Ni^{2+}$, and NaOH-$Fe^{3+}Ni^{2+}$. F) Observation of pH as a function of time for solutions containing different metal cations.

aforementioned morphology difference. The X-ray diffraction (XRD) pattern of $NH_3$-$Fe^{2+}Ni^{2+}$ in Figure 1E shows three diffraction peaks at $2\theta$ values of 11.6, 23.3, and 34.5°, corresponding to the d-values of 7.6, 3.8, and 2.6 Å, respectively. The d-values correspond to the (003), (006), and (009) planes of the hydrotalcite-like structure, respectively, confirming the successful formation of LDHs.[11] In contrast, β-$Ni(OH)_2$ is obtained in the case of $NH_3$-$Fe^{3+}Ni^{2+}$, and FeNi-LDH is obtained in the cases of NaOH-$Fe^{2+}Ni^{2+}$ and NaOH-$Fe^{3+}Ni^{2+}$. Note that the sharp and intense diffraction peaks of $NH_3$-$Fe^{2+}Ni^{2+}$ and $NH_3$-$Fe^{3+}Ni^{2+}$ indicate their highly crystalline nature, and the broad diffraction peaks of NaOH-$Fe^{2+}Ni^{2+}$ and NaOH-$Fe^{3+}Ni^{2+}$ suggest their poor crystallinity. The crystalline difference is confirmed by the fast Fourier transform (FFT) patterns obtained from their high-resolution TEM (HRTEM) images (Figure S2). Overall, varying alkaline sources has a greater influence on the morphology and crystallinity than changing Fe species, while the incorporation of Fe species into the lattice of $Ni(OH)_2$ is strongly associated with the selection of both Fe species and alkaline sources.

Theoretically, the hydroxide's formation process can be described as follows (Figure S3): (1) M first interacts with water molecules to form the hexaaqua ions $[M(H_2O)_6]^{n+}$. (2) As the pH rises, $[M(H_2O)_6]^{n+}$ undergoes a deprotonation process, condensation reactions via olation or oxolation, and elimination of water molecules, leading to the formation of an insoluble hydroxide network.[12] The formation of FeNi-LDHs additionally involves the incorporation and the acceptance of $[Fe(H_2O)_6]^{2+/3+}$ into the $Ni(OH)_2$ network. Since the whole process is driven by the change of OH$^-$ concentration, observing pH as a function of time (Figure S4) is a suitable way to investigate the influence of varying Fe species or alkaline sources on the formation of FeNi-LDHs. We first recorded the pH profile of $NH_3$ diffusing into an aqueous solution of 20 mM $Ni^{2+}$, 20 mM $Fe^{2+}$, and 20 mM $Fe^{3+}$. As shown in Figure 1F, these pH profiles could be divided into several corresponding stages.



**Scheme 1.** A schematic illustration of four reaction routes.

Concretely, their pH profiles show an increasing trend during the first stage caused by the hydrolysis of $NH_3 \cdot H_2O$. Then, the pH curves reach a constant plateau, meaning that an equal rate is obtained for the generation of $OH^-$ and its consumption by the hydrolysis of M. Note that the pH values of these plateaus are different, which is consistent with the hydrolysis behavior difference of these cations. Subsequently, before reaching the final plateau, the pH curves display again a rapid rise, indicating that the generation rate of $OH^-$ is faster than the consumption rate of $OH^-$, which results from the nearly completed hydrolysis of M. The pH profile of $NH_3$-$Fe^{2+}Ni^{2+}$ exhibits also a similar multi-staged change. The presence of the only plateau that is located between the plateaus of $NH_3$-$Ni^{2+}$ and $NH_3$-$Fe^{2+}$ evidences the synchronized deprotonation and condensation reaction of $Fe^{2+}$ and $Ni^{2+}$ hexaaqua ions, which is beneficial for the incorporation of $[Fe(H_2O)_6]^{2+}$ into the $Ni(OH)_2$ network. In contrast, the pH profile of $NH_3$-$Fe^{3+}Ni^{2+}$ displays two plateaus at pH of 2.8 and 8.9, which correspond to the hydrolysis of $Fe^{3+}$ and $Ni^{2+}$, respectively, suggesting their respective or staged hydrolysis. As for pH profiles of $NaOH$-$Fe^{2+}Ni^{2+}$ and $NaOH$-$Fe^{3+}Ni^{2+}$, before reaching the final chemical equilibrium, their pH immediately increases to around 12 at the moment of adding NaOH aqueous solution due to the instant release of $OH^-$. Based on the above results, it is concluded that

(1) $Fe^{3+}$ hydrolyses fast while $Ni^{2+}$ and $Fe^{2+}$ have considerably slower and similar hydrolysis behavior.

(2) For $NH_3$ diffusion, the successful formation of FeNi-LDHs took place in the case of $Fe^{2+}/Ni^{2+}$, instead of $Fe^{3+}/Ni^{2+}$, which is caused by the synchronized or staged hydrolysis, indicating that, under the low change rate of $OH^-$ concentration, the hydrolysis behavior difference between $Ni^{2+}$ and $Fe^{2+/3+}$ can change the possibility of the incorporation and the acceptance of $[Fe(H_2O)_6]^{2+/3+}$ into the $Ni(OH)_2$ network, which in turn influences the formation of FeNi-LDHs.

(3) Utilizing NaOH aqueous solution as the alkaline source preferentially promotes the formation of FeNi-LDHs regardless of the Fe species, which can be attributed to the condition that the instant increase of $OH^-$ concentration results in the compulsive incorporation of $[Fe(H_2O)_6]^{2+/3+}$ into the $Ni(OH)_2$ network. Meanwhile, the $Ni(OH)_2$ network tends to accept these $[Fe(H_2O)_6]^{2+/3+}$ ions owing to the insufficient time for $[Fe(H_2O)_6]^{3+}$ and $[Ni(H_2O)_6]^{2+}$ to exchange/rearrange before olation.

The above results disclosed how varying Fe species and the real-time change of $OH^-$ concentration influence the morphology, crystallinity, and the incorporation of Fe species into the lattice of $Ni(OH)_2$, guiding us to design the synthesis scheme for LDHs with the desired attributes.

Since the composition of LDHs exerts a vital influence on their performance, we were interested to extend our synthesis method to more LDHs. We focused on the strategy of preparing $NH_3$-$Fe^{2+}Ni^{2+}$ because it not only possesses high crystallinity and well-defined morphology but also exhibits better OER activity than $NH_3$-$Fe^{3+}Ni^{2+}$, $NaOH$-$Fe^{2+}Ni^{2+}$, and $NaOH$-$Fe^{3+}Ni^{2+}$ (Figure S5). Besides,

the facile synthesis condition and the upscaling possibility to the gram range (Figure S6) are clear advantages for facilitating the low-cost fabrication of such material compared with other reported methods (Figure 2A and Table S1). Accordingly, a series of experiments with a Fe/Ni ratio ranging from 100/0 to 0/100 was conducted, and the obtained nanomaterials were denoted as $NH_3$-$Fe^{2+}Ni^{2+}$-FexNiy. X-ray photoelectron spectroscopy (XPS) was used to characterize the composition of these nanomaterials. The Fe/Ni ratio is calculated and the results are in good agreement with the feeding ratios (Figure 2C). The XRD patterns (Figure 2D) of the nanomaterials with Fe/Ni feeding ratio = 100/0, 99/1, and 90/10 are indexed to $\gamma$-$Fe_2O_3$.[13] The XRD pattern of $NH_3$-$Fe^{2+}Ni^{2+}$-Fe75Ni25 is similar to that of 100/0 except for an additional weak signal at 11.5° belonging to the (003) facet of $\alpha$-$Ni(OH)_2$, suggesting that $\gamma$-$Fe_2O_3$ can only tolerate a certain amount of $Ni^{2+}$. Interestingly, with a further decrease in Fe/Ni, the main characteristic peaks of $NH_3$-$Fe^{2+}Ni^{2+}$-Fe50Ni50 are assigned to different facets of $\alpha$-$Ni(OH)_2$ besides a weak peak at around 35.6° resulting from $\gamma$-$Fe_2O_3$. In the XRD pattern of $NH_3$-$Fe^{2+}Ni^{2+}$-Fe25Ni75, it is found that $\alpha$-$Ni(OH)_2$ is still the main phase, and traces of $\beta$-$Ni(OH)_2$ instead of the $\gamma$-$Fe_2O_3$ phase are also observed. This phenomenon demonstrates that an insufficient amount of Fe dopant leads to the formation of pure $\beta$-$Ni(OH)_2$. Further decreasing the doping amount of Fe results in the increase of the peak intensity at 19.2° and the decrease of the peak intensity at 11.5°, implying the quantity change of $\beta$-$Ni(OH)_2$ and $\alpha$-$Ni(OH)_2$ phases. Besides, as shown in Figure S7, changing Fe/Ni ratio affects the morphology of the synthesized nanomaterials. Note that we also demonstrate the successful transfer of our synthesis strategy to LDHs of CoY, FeY, CoNi and CoNiY.
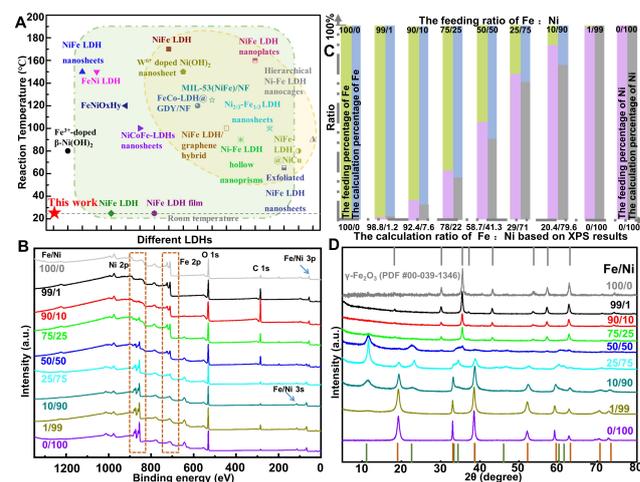


***Figure 2.*** A) A comparison of our synthesis process compared to other reported synthesis processes. The synthesis processes highlighted in green and yellow involve the use of special devices and organic solvents, respectively. B) XPS spectra of the as-prepared nanomaterials with various Fe/Ni feeding ratios. C) The feeding percentage and the calculation percentage of Fe: Ni. D) XRD patterns of the as-prepared nanomaterials with various Fe/Ni feeding ratios.

As seen in Figure S13 and Figure 3A, $NH_3$-$Fe^{2+}Ni^{2+}$-Fe25Ni75 has the lowest overpotential of 203 mV for OER at 10 mA cm$^{-2}$. Besides, the calculated Tafel slope value of $NH_3$-$Fe^{2+}Ni^{2+}$-Fe25Ni75 is as low as 24.9 mV dec$^{-1}$ (Figure 3B), indicating its faster charge transfer. Note that the remarkable OER performance of $NH_3$-$Fe^{2+}Ni^{2+}$-Fe25Ni75 is better than the reference samples of this work and reported congeneric materials (Figure 3C and Table S3).[1d,14] To further evaluate its intrinsic activity, turnover frequencies (TOFs) and the double-layer capacitance ($C_{dl}$) were analyzed. As shown in Figure 3D and S14A–E, the highest

double-layer capacitance value (5.89 mF cm$^{-2}$) and turnover frequencies value (0.015 s$^{-1}$ at the overpotential of 240 mV) of $NH_3$-$Fe^{2+}Ni^{2+}$-Fe25Ni75 further confirms that it affords the large electrochemically active surface area and excellent intrinsic activity toward catalyzing OER. As presented in Figure S14F, the potential for each step at different current densities could maintain constant for 1000 s, suggesting its excellent stability and mass transport performance. Furthermore, the potential remains nearly constant at a current density of 10 mA cm$^{-2}$ for 100 h (Figure S15A) and 100 mA cm$^{-2}$ for 24 h (Figure S15B), again indicating excellent long-term stability. Note that such good stability is also supported by a negligible dissolution of Fe and Ni content (Table S4) captured in the used electrolyte after a long-term stability test over 100 h via the inductively coupled plasma mass spectrometry.

The selected area electron diffraction (SAED) result (Figure 4A) reveals its single-crystalline nature and the exposed (001) planes, which is further confirmed by the HRTEM image (Figure 4B) showing clear lattice fringes with a lattice spacing of 0.154 nm. To determine the exact thickness, we observed $NH_3$-$Fe^{2+}Ni^{2+}$-Fe25Ni75 from the direction parallel to the lateral surface by using scanning transmission electron microscopy (STEM). The result in Figure 4C suggests that its thickness is 2–8 nm. EDX indicates the co-existence of Fe/Ni elements and their homogeneous distribution on the micrometer and nanometer (Figure 4D–F and S16) length scales. Multivariate statistical analysis[15] did not reveal the segregation of Fe or Ni. These features are beneficial for exposing more active sites that can be contacted with the electrolyte. Besides, XPS was employed to analyze the valence state and electronic structure. The Ni 2p spectrum (Figure 4H) presents two main peaks located at around 856 and 874 eV, corresponding to the $Ni^{2+}$ oxidation state. In the Fe 2p spectrum (Figure 4I), two main peaks at 711.4 and 725.8 eV reveal the $Fe^{3+}$ oxidation state, and the pre-peak at around 707 eV is attributed to the presence of Fe species with a lower-than-normal oxidation state.[16] The shift towards higher values of the binding energy of Fe 2p and Ni 2p in $NH_3$-$Fe^{2+}Ni^{2+}$-Fe25Ni75 compared to that of $NH_3$-$Fe^{2+}Ni^{2+}$-Fe0Ni100 and $NH_3$-$Fe^{2+}Ni^{2+}$-Fe100Ni0 signifies the mutual effect between Fe species and Ni species in $NH_3$-$Fe^{2+}Ni^{2+}$-Fe25Ni75. Such coupling could improve OER kinetics by modulating the electronic structure to accelerate electron transfer from the electrode to reactants.[7c,17]

X-ray absorption spectroscopy (XAS) was employed to further clarify the local fine structure, atomic coordination, and bond lengths of the relevant samples. As shown in Figure 5A and B, the pre-edge intensity increase of $NH_3$-$Fe^{2+}Ni^{2+}$-Fe25Ni75 indicates a completely unsaturated 6-coordinate Ni structure, and the pre-edge exhibiting a substantial shift to the higher energy compared with that of commercial and synthesized Ni(OH)$_2$ suggests the increase in the oxidation state of Ni species, in agreement with the aforementioned XPS result. Meanwhile, the normalized Fe K-edge XAS spectrum (Figure 5D and E) shows a weak shift of the absorption edge toward lower energies with respect to Fe$_2$O$_3$, suggesting the decreased oxidation state of
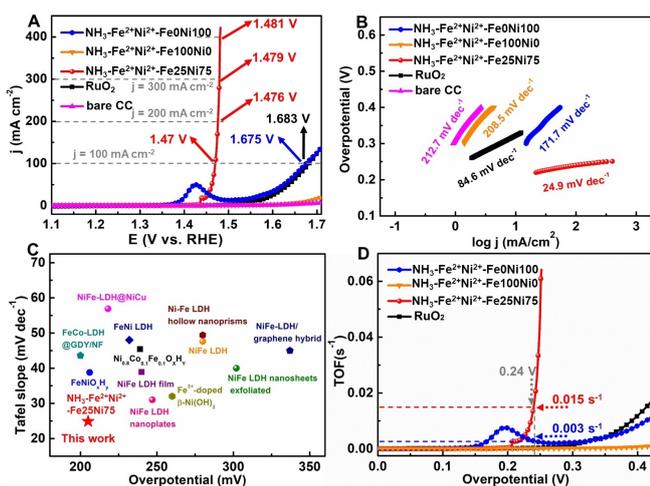


**Figure 3.** A) Linear sweep voltammetry (LSV) curves and B) Tafel slopes of different materials. C) Comparison of OER overpotential (10 mA cm$^{-2}$) and Tafel slope of $NH_3$-$Fe^{2+}Ni^{2+}$-Fe25Ni75 with reported catalysts. D) TOF of different materials.
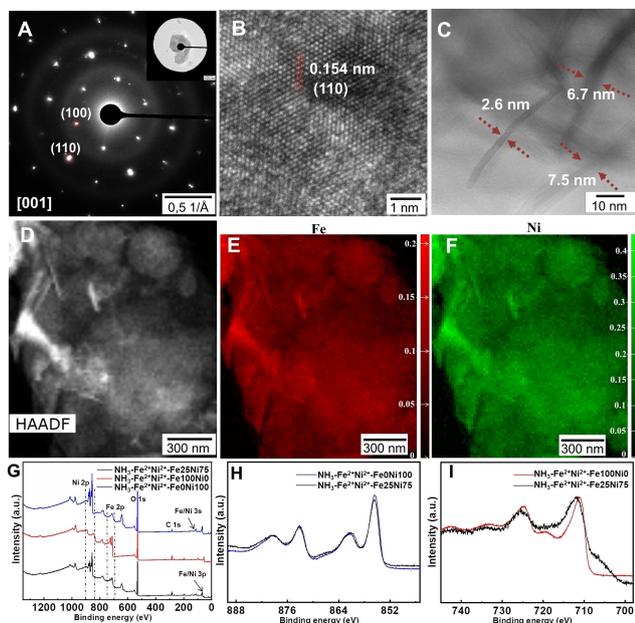


**Figure 4.** A) SAED pattern, B) HRTEM image, C), D) STEM images of $NH_3$-$Fe^{2+}Ni^{2+}$-Fe25Ni75. Multivariate statistical analysis for E) Fe and F) Ni. G) XPS survey spectra, H) Ni 2p spectra, and I) Fe 2p spectra.
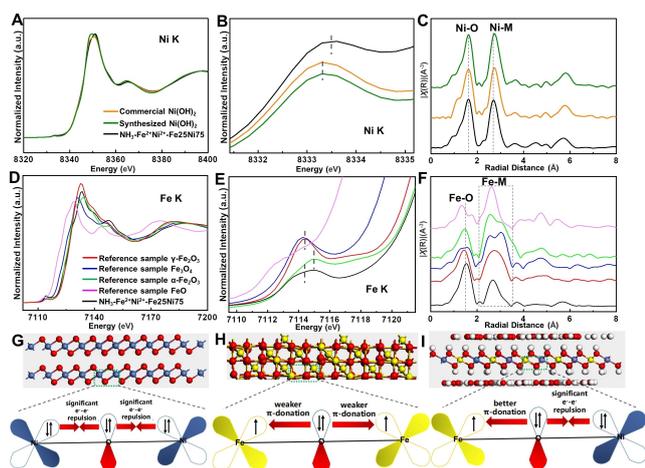
**Figure 5.** Normalized (A and B) Ni and (D and E) Fe K-edge XANES spectra. Fourier-transformed EXAFS curves at C) Ni and F) Fe K-edge. G)–I) Atomic structure and schematic representation of the electronic coupling.

Fe species. The above-mentioned change in the oxidation state of Ni and Fe species is due to the partial electron transfer from $Ni^{2+}$ to $Fe^{3+}$ through the oxygen bridge (Figure 5G–I).[18] Such electron transfer will induce a change in $e_g$ filling of Ni species, which could reform the local electronic structure and change the reaction behavior of $H_2O$, intermediates, and $O_2$ in the OER process, hence leading to enhanced OER activity. Figure 5C and F show the Fourier-transformed extended X-ray absorption fine structure (EXAFS) of Ni/Fe K-edge. Compared with those in the synthesized and commercial $Ni(OH)_2$ samples, the Ni–O at around 1.6 Å and Ni–M bonds at around 2.69 Å in $NH_3$-$Fe^{2+}Ni^{2+}$-Fe25Ni75 present a shorter radial distance, which is consistent with its higher oxidation-state-sensitive energy shown in the X-ray absorption near-edge structure (XANES) spectra. Based on the above analysis, we infer that the local electronic structure change of Ni sites caused by the incorporation of Fe species is responsible for improving the electrocatalysis performance, which is supported by the increase of oxidation state and the change of local coordination environment for $NH_3$-$Fe^{2+}Ni^{2+}$-Fe25Ni75 evidenced by TEM, XPS and XANES results (Figure S17) after OER stability. Besides, the positive effect of the incorporation of Fe species on boosting the catalytic OER activity is confirmed by DFT calculations (Figure S18). To be specific, both the FeNi-LDH and β-$Ni(OH)_2$ afford the same rate-determining step of the formation of OOH* from O*. Gibbs free formation energies results indicate that the FeNi-LDH requires a lower overpotential of 0.35 V than β-$Ni(OH)_2$ (0.56 V), decoding the better OER activity of the FeNi-LDH. To further unravel the underlying mechanism for the promoted activity of the FeNi-LDH, we have carried out a Bader charge analysis. The Bader charge for the incorporated Fe is +1.99 e, much higher as compared to Ni species (+1.36 e) in β-$Ni(OH)_2$. This largely weakens the binding energy of O* by 0.29 eV, while moderately weakening the binding energy of OOH* by 0.08 eV. The whole

effect thus reduces the formation energy of OOH* from O* by 0.21 eV.

## Conclusion

Here, the deliberately designed combination of $NH_3$ gas diffusion and in situ pH measurement provides a solution for investigating the formation mechanism of FeNi-LDHs. The obtained results demonstrated that the incorporation of Fe species into $Ni(OH)_2$ lattice is influenced by the hydrolysis behavior difference between $Ni^{2+}$ and $Fe^{2+/3+}$ under the low change rate of $OH^-$, while the rapid increase of $OH^-$ concentration can promote the successful formation of FeNi-LDHs regardless of the Fe species. Furthermore, we disclosed that adjusting the change rate of $OH^-$ can tune the morphology, crystallinity, and purity of the obtained FeNi-LDHs. Under the guidance of our findings, the same strategy was successfully extended to prepare other binary or ternary LDHs. After evaluating the OER performance of all obtained products, it is found that $NH_3$-$Fe^{2+}Ni^{2+}$-Fe25Ni75 exhibits one of the best OER performances so far reported. This work takes one step forward towards in situ investigations of the formation mechanism of LDHs and the corresponding findings can provide further opportunities not only to improve the synthesis condition of LDHs but also to realize the customized synthesis of LDHs with the desired features.

## Conflict of Interest

The authors declare no conflict of interest.

## Data Availability Statement

The data that support the findings of this study are available from the corresponding author upon reasonable request.

**Keywords:** Formation Mechanism · Layered Double Hydroxide · $OH^-$ Concentration · Oxygen Evolution Reaction · In Situ Characterization

*Angewandte*
International Edition *Chemie*

[1] a) L. Lv, Z. Yang, K. Chen, C. Wang, Y. Xiong, *Adv. Energy Mater.* **2019**, *9*, 1803358; b) A. R. Sotiles, L. M. Baika, M. T. Grassi, F. Wypych, *J. Am. Chem. Soc.* **2019**, *141*, 531–540; c) J. Yu, Q. Wang, D. O'Hare, L. Sun, *Chem. Soc. Rev.* **2017**, *46*, 5950–5974; d) L. Yu, J. F. Yang, B. Y. Guan, Y. Lu, X. W. Lou, *Angew. Chem. Int. Ed.* **2018**, *57*, 172–176; *Angew. Chem.* **2018**, *130*, 178–182; e) J. Zhang, L. Yu, Y. Chen, X. F. Lu, S. Gao, X. W. Lou, *Adv. Mater.* **2020**, *32*, 1906432.

[2] a) J. Zhang, J. Liu, L. Xi, Y. Yu, N. Chen, S. Sun, W. Wang, K. M. Lange, B. Zhang, *J. Am. Chem. Soc.* **2018**, *140*, 3876–3879; b) F. Dionigi, J. Zhu, Z. Zeng, T. Merzdorf, H. Sarodnik, M. Gliech, L. Pan, W. X. Li, J. Greeley, P. Strasser, *Angew. Chem. Int. Ed.* **2021**, *60*, 14446–14457; *Angew. Chem.* **2021**, *133*, 14567–14578; c) D. Wang, Q. Li, C. Han, Q. Lu, Z. Xing, X. Yang, *Nat. Commun.* **2019**, *10*, 3899; d) K. He, T. Tadesse Tsega, X. Liu, J. Zai, X. H. Li, X. Liu, W. Li, N. Ali, X. Qian, *Angew. Chem. Int. Ed.* **2019**, *58*, 11903–11909; *Angew. Chem.* **2019**, *131*, 12029–12035; e) X. Zhang, Y. Zhao, Y. Zhao, R. Shi, G. I. Waterhouse, T. Zhang, *Adv. Energy Mater.* **2019**, *9*, 1900881; f) J. Kang, X. Qiu, Q. Hu, J. Zhong, X. Gao, R. Huang, C. Wan, L. M. Liu, X. Duan, L. Guo, *Nat. Catal.* **2021**, *4*, 1050–1058; g) Y. Zhao, L. Zheng, R. Shi, S. Zhang, X. Bian, F. Wu, X. Cao, G. I. Waterhouse, T. Zhang, *Adv. Energy Mater.* **2020**, *10*, 2002199; h) W. Yu, N. Deng, K. Cheng, J. Yan, B. Cheng, W. Kang, *J. Energy Chem.* **2021**, *58*, 472–499; i) J. Hu, X. Tang, Q. Dai, Z. Liu, H. Zhang, A. Zheng, Z. Yuan, X. Li, *Nat. Commun.* **2021**, *12*, 3409; j) V. A. Shirin, R. Sankar, A. P. Johnson, H. Gangadharappa, K. Pramod, *J. Controlled Release* **2021**, *330*, 398–426; k) Z. Cao, B. Li, L. Sun, L. Li, Z. P. Xu, Z. Gu, *Small Methods* **2020**, *4*, 1900343; l) N. Baig, M. Sajid, *Trends Environ. Anal. Chem.* **2017**, *16*, 1–15; m) X. Qiao, X. Chen, C. Huang, A. Li, X. Li, Z. Lu, T. Wang, *Angew. Chem. Int. Ed.* **2019**, *58*, 16523–16527; *Angew. Chem.* **2019**, *131*, 16675–16679.

[3] a) Y. Lin, H. Wang, C. K. Peng, L. Bu, C. L. Chiang, K. Tian, Y. Zhao, J. Zhao, Y. G. Lin, J. M. Lee, *Small* **2020**, *16*, 2002426; b) M. Gong, Y. Li, H. Wang, Y. Liang, J. Z. Wu, J. Zhou, J. Wang, T. Regier, F. Wei, H. Dai, *J. Am. Chem. Soc.* **2013**, *135*, 8452–8455; c) L. Dang, H. Liang, J. Zhuo, B. K. Lamb, H. Sheng, Y. Yang, S. Jin, *Chem. Mater.* **2018**, *30*, 4321–4330.

[4] L. Yu, H. Zhou, J. Sun, F. Qin, F. Yu, J. Bao, Y. Yu, S. Chen, Z. Ren, *Energy Environ. Sci.* **2017**, *10*, 1820–1827.

[5] a) N. T. Thanh, N. Maclean, S. Mahiddine, *Chem. Rev.* **2014**, *114*, 7610–7630; b) H. X. Lin, Z. C. Lei, Z. Y. Jiang, C. P. Hou, D. Y. Liu, M. M. Xu, Z. Q. Tian, Z. X. Xie, *J. Am. Chem. Soc.* **2013**, *135*, 9311–9314; c) W. H. Lai, Y. X. Wang, Y. Wang, M. Wu, J. Z. Wang, H. K. Liu, S. L. Chou, J. Chen, S. X. Dou, *Nat. Chem.* **2019**, *11*, 695–701; d) I. Sunagawa, *Crystals: growth, morphology, & perfection*, Cambridge University Press, Cambridge, **2005**; e) C. Yuan, A. Levin, W. Chen, R. Xing, Q. Zou, T. W. Herling, P. K. Challa, T. P. Knowles, X. Yan, *Angew. Chem. Int. Ed.* **2019**, *58*, 18116–18123; *Angew. Chem.* **2019**, *131*, 18284–18291; f) J. J. De Yoreo, P. U. Gilbert, N. A. Sommerdijk, R. L. Penn, S. Whitelam, D. Joester, H. Zhang, J. D. Rimer, A. Navrotsky, J. F. Banfield, *Science* **2015**, *349*, 6247, aaa6760.

[6] a) X. Yan, Q. T. Hu, G. Wang, W. D. Zhang, J. Liu, T. Li, Z. G. Gu, *Int. J. Hydrogen Energy* **2020**, *45*, 19206–19213; b) D. Ma, B. Hu, W. Wu, X. Liu, J. Zai, C. Shu, T. T. Tsega, L. Chen, X. Qian, T. L. Liu, *Nat. Commun.* **2019**, *10*, 3367; c) X. Zheng, X. Han, Y. Cao, Y. Zhang, D. Nordlund, J. Wang, S. Chou, H. Liu, L. Li, C. Zhong, *Adv. Mater.* **2020**, *32*, 2000607.

[7] a) K. Zhu, H. Liu, M. Li, X. Li, J. Wang, X. Zhu, W. Yang, *J. Mater. Chem. A* **2017**, *5*, 7753–7758; b) Y. Zhang, C. Wu, H. Jiang, Y. Lin, H. Liu, Q. He, S. Chen, T. Duan, L. Song, *Adv. Mater.* **2018**, *30*, 1707522; c) F. Dionigi, Z. Zeng, I. Sinev, T. Merzdorf, S. Deshpande, M. B. Lopez, S. Kunze, I. Zegkinoglou, H. Sarodnik, D. Fan, *Nat. Commun.* **2020**, *11*, 2522.

[8] a) M. G. Page, H. Cölfen, *Cryst. Growth Des.* **2006**, *6*, 1915–1920; b) A. W. Xu, M. Antonietti, H. Cölfen, Y. P. Fang, *Adv. Funct. Mater.* **2006**, *16*, 903–908; c) S. Sun, D. M. Chevrier, P. Zhang, D. Gebauer, H. Cölfen, *Angew. Chem. Int. Ed.* **2016**, *55*, 12206–12209; *Angew. Chem.* **2016**, *128*, 11939–11943; d) Z. Chen, X. Wang, S. Keßler, Q. Fan, M. Huang, H. Cölfen, *J. Energy Chem.* **2022**, *71*, 89–97.

[9] a) Q. Han, Y. Luo, J. Li, X. Du, S. Sun, Y. Wang, G. Liu, Z. Chen, *Appl. Catal. B* **2022**, *304*, 120937; b) G. Chen, H. Wan, W. Ma, N. Zhang, Y. Cao, X. Liu, J. Wang, R. Ma, *Adv. Energy Mater.* **2020**, *10*, 1902535.

[10] a) I. Roger, M. A. Shipman, M. D. Symes, *Nat. Chem. Rev.* **2017**, *1*, 0003; b) F. Dionigi, P. Strasser, *Adv. Energy Mater.* **2016**, *6*, 1600621; c) P. Zhai, M. Xia, Y. Wu, G. Zhang, J. Gao, B. Zhang, S. Cao, Y. Zhang, Z. Li, Z. Fan, *Nat. Commun.* **2021**, *12*, 457.

[11] Y. Zhu, H. Li, Y. Koltypin, A. Gedanken, *J. Mater. Chem.* **2002**, *12*, 729–733.

[12] M. Henry, J. P. Jolivet, J. Livage, *Chemistry, Spectroscopy and Applications of Sol-Gel Glasses*, Springer Berlin Heidelberg, Berlin, **1992**, pp. 153–206.

[13] E. Darezereshki, *Mater. Lett.* **2010**, *64*, 1471–1472.

[14] a) Q. Zhao, J. Yang, M. Liu, R. Wang, G. Zhang, H. Wang, H. Tang, C. Liu, Z. Mei, H. Chen, *ACS Catal.* **2018**, *8*, 5621–5629; b) L. Hui, Y. Xue, B. Huang, H. Yu, C. Zhang, D. Zhang, D. Jia, Y. Zhao, Y. Li, H. Liu, *Nat. Commun.* **2018**, *9*, 5309; c) Y. Zhou, Z. Wang, Z. Pan, L. Liu, J. Xi, X. Luo, Y. Shen, *Adv. Mater.* **2019**, *31*, 1806769.

[15] S. Zhang, C. Scheu, *Microscopy* **2018**, *67*, i133–i141.

[16] Z. Wan, Z. Ma, H. Yuan, K. Liu, X. Wang, *ACS Appl. Energy Mater.* **2022**, *5*, 4603–4612.

[17] a) S. Zhao, Y. Wang, J. Dong, C. T. He, H. Yin, P. An, K. Zhao, X. Zhang, C. Gao, L. Zhang, J. Lv, J. Wang, J. Zhang, A. M. Khattak, N. A. Khan, Z. Wei, J. Zhang, S. Liu, H. Zhao, Z. Tang, *Nat. Energy* **2016**, *1*, 16184; b) C. Kuai, C. Xi, A. Hu, Y. Zhang, Z. Xu, D. Nordlund, C. J. Sun, C. A. Cadigan, R. M. Richards, L. Li, *J. Am. Chem. Soc.* **2021**, *143*, 18519–8526.

[18] a) M. W. Louie, A. T. Bell, *J. Am. Chem. Soc.* **2013**, *135*, 12329–12337; b) J. Y. Chen, L. Dang, H. Liang, W. Bi, J. B. Gerken, S. Jin, E. E. Alp, S. S. Stahl, *J. Am. Chem. Soc.* **2015**, *137*, 15090–15093.